

An Easy Route to Synthesize Novel Fe₃O₄@Pt Core-shell Nanostructures with High Electrocatalytic Activity

Nora Mayté Sánchez-Padilla¹, Sagrario M. Montemayor^{1,*} and F.J. Rodríguez Varela^{2,†}

¹Universidad Autónoma de Coahuila, V. Carranza s/n, Saltillo, Coahuila, México, CP 25280

²Grupo de Recursos Naturales y Energéticos, CINVESTAV Unidad Saltillo,
Carr. Saltillo-Monterrey km. 13.5, Ramos Arizpe, Coahuila, México, CP 25900

Received: December 20, 2011, Accepted: February 13, 2012, Available online: April 16, 2012

Abstract: In this work, the effect of changing the stirring method and temperature on the physicochemical properties of metallic nanoparticles and core-shell nanostructures is shown. Magnetic (MS), mechanical (UT) and ultrasonic (USS) stirring are the methods of synthesis. The effect that, temperatures between 0 and 50 °C, has on the structure and particle size of Fe₃O₄ nanoparticles is evaluated. The results indicate that Fe₃O₄ prepared by the three methods presents a spinel-type crystalline structure. An increase in the synthesis temperature leads to highly crystalline powders. Afterwards, Pt is deposited by the UT method on Fe₃O₄ to form Fe₃O₄@Pt core-shell nanostructures. It is important to mention that the time used for the synthesis of the nanoparticles and the core-shell nanostructures is only one minute. The presence of Fe₃O₄ and Pt is confirmed by XRD and XPS. The metallic Pt phase is confirmed because the binding energy of Pt 4f^{7/2} is associated to platinum in the zero-valent state. We evaluated the electrochemical activity of the Fe₃O₄@Pt core-shell nanostructures for the oxygen reduction reaction (ORR). The novel materials show a high electrocatalytic activity and the Koutecky-Levich analysis indicates that the reaction follows a 4 electron transfer mechanism on the Fe₃O₄@Pt nanostructures prepared by the three stirring processes. Moreover, the mass specific activity of the core-shell materials is as high as that obtained from the Pt-alone catalysts, suggesting that the amount of Pt in these electrodes can be reduced without decreasing the performance.

Keywords: electrocatalysts, core-shell nanostructures, magnetite-Pt, ORR

1. INTRODUCTION

Worldwide, much attention has been paid to the synthesis and characterization of bimetallic nanostructures due to the possibility that catalytic properties of such materials can be tailored by changes in their composition and morphology. Some technological areas which can benefit from a good control in the composition, structure and size of the bimetallic materials are catalytic reforming, pollution control and electrocatalysis in fuel cells. It is well known that the chemical composition and the structure, especially on the surface of materials, can be modified by changing reaction conditions. This, in the nanometric scale, leads to exponential changes because of the large surface/size relationship. There are several ways to synthesize metallic nanoparticles and bimetallic nanostructures which involve the use of multiple steps of heating, handling and purification of the intermediates and products [1-3].

From an application point of view, systems having bimetallic, core-shell or pseudo-core-shell structures, with high catalytic activity and electrochemical stability as anodes or cathodes for low temperature fuel cells have been developed recently by different synthesis routes [4-6]. Core-shell materials such as Pd@Pt or Pt@Pd [2, 3, 4, 7], Ni@Pt [5], PdCu@Pt [6], PdCo@Pt [8], Ru@PtPd [9], Ru@Pt [10], among other structures, are being tested with success in the field of electrocatalysis. It has been demonstrated that the formation of the core-shell nanostructures can enhance the electrochemical catalytic activity of anodes or cathodes for fuel cells applications [5, 11].

In the course to find a simple synthesis method to obtain metallic nanoparticles and bimetallic nanostructures, which will allow us to have a good control of the structure and to obtain materials with improved catalytic properties, herein we report the effect of the stirring method (MS, UT and USS) and the temperature on the synthesis of spinel-type Fe₃O₄ nanoparticles from Fe(NO₃)₃·9H₂O

To whom correspondence should be addressed:
Email: *smmontemayor@gmail.com, †javier.varela@cinvestav.edu.mx

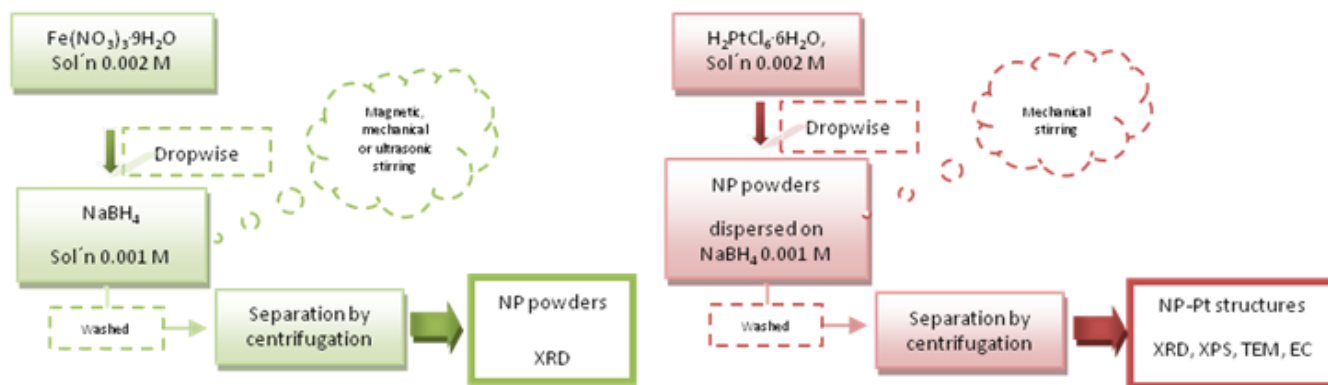


Figure 1. Flowchart of the experimental procedure to obtain nanoparticles (left) and nanoparticles-Pt (right).

precursor by using NaBH₄ as reducing agent. Then, a Pt shell is deposited on the iron oxides by the reduction of chloroplatinic acid hexahydrate (H₂PtCl₆) also with NaBH₄. We aim to obtain Fe₃O₄@Pt core-shell nanostructures and to evaluate their catalytic activity as cathode materials for the ORR in acid medium. It is important to mention that the time used for the synthesis, both of nanoparticles (cores) and core-shell nanostructures is very short, i.e., only one minute. The results prove that the time invested in the synthesis of fuel cell catalysts can be significantly reduced and still it is possible to produce nanostructures with high catalytic activity.

2. EXPERIMENTAL

2.1. Synthesis of nanoparticles and core-shell nanostructures

The reagents used to obtain the nanomaterials were Fe(NO₃)₃·9H₂O and H₂PtCl₆·6H₂O as metallic sources, NaBH₄ as reducing agent. H₂SO₄ was used as electrolyte. All chemicals were purchased from Aldrich. In a typical synthesis process, the stoichiometric amount of a 0.002 M metallic salt solution was added dropwise into a 0.001 M NaBH₄ solution at 25 °C (RT, room temperature). Each one of the salts was added into the reducing agent under three different types of stirring: MS, UT or USS. In the case of Pt-alone nanoparticles, we considered the same stoichiometry, although the synthesis was carried out by UT only. The particles obtained were washed and separated by centrifugation at 300 rpm. Then, the powders were characterized by XRD to determine the structural parameters and crystallite size.

After obtaining such iron oxide nanoparticles (cores), Fe₃O₄@Pt core-shell materials were prepared with a nominal Fe₃O₄:Pt weight ratio of 1:1. An appropriate amount of 0.002 M H₂PtCl₆·6H₂O solution was added dropwise into a 0.001 M NaBH₄ solution which contained 0.1 g of the core powders under UT stirring. The core-shell structures were characterized by XRD, XPS, EDX and TEM and electrochemical techniques. Figure 1 shows a schematic diagram of the experimental procedure followed during the synthesis of Fe₃O₄, Pt and Fe₃O₄-Pt nanostructures.

2.2. Preparation of working electrodes and electrochemical characterization

We have described previously the preparation of the working electrodes [12, 13]. A catalytic ink was prepared by mixing 20 mg

of the corresponding catalyst, 2 mL deionized water and 20 μL of Nafion (5 % wt, DuPont) by ultrasound, to form an ink of 10 mg_{catal}/mL. Then, an aliquot of 10 μL of the solution was dispersed onto a 0.196 cm² geometrical area glassy carbon disc (mirror polished with 0.05 mm alumina) fixed in an electrode support.

Activation of the nanostructures was performed by cyclic voltammetry (CV). Potential cycles were taken at 50 mV/s in N₂-saturated 0.5 M H₂SO₄ in the 0.05 to 1.2 V vs SHE potential interval, with the aid of a potentiostat (Voltalab) connected to a RDE instrument (Pine Inst.). It was found that 40 cycles were sufficient to obtain reproducible voltammograms. After activation, CVs presented in this work were acquired at the scan rate of 20 mV/s. Then, the catalytic activity for the ORR of the core@shell nanostructures was evaluated. Linear Scan Voltammograms (LSV) were collected in the cathodic direction at the slow scan rate of 2 mV/s in the same potential interval as in the CV measurements, with the RDE operating at 400, 800, 1200, 1600 and 2000 rpm. The counter electrode was a Pt mesh and we used an Ag/AgCl reference electrode, although all potentials are reported here against the Standard Hydrogen Electrode (SHE). All electrochemical experiments were performed at RT.

3. RESULTS AND DISCUSSION

The first evidence of the effect of NaBH₄ on the metallic salts is the formation of a black colloidal suspension. This happened using any of both metallic salts (Fe³⁺ or Pt⁴⁺) and the three stirring methods.

Figure 2 shows the XRD patterns of powders obtained with the different stirring methods, labeled as Fe₃O₄-MS, Fe₃O₄-UT and Fe₃O₄-USS, respectively. A spinel-type cubic phase identified as magnetite (FeO·Fe₂O₃, PDF 89-0691) is present in all cases, although the intensity of the reflections is lower or higher as a function of the stirring method. An additional peak ascribed to NaNO₃ appears in the diffractogram of Fe₃O₄-UT and is related to a secondary phase not completely washed out during the recovery of the material.

The crystallite sizes, calculated using the Scherrer equation, are in the range of 5 to 8 nm, the largest one being that of the Fe₃O₄-USS nanoparticles. The small crystallite size of Fe₃O₄ obtained with the three stirring methods is in agreement with the RT used during the synthesis.

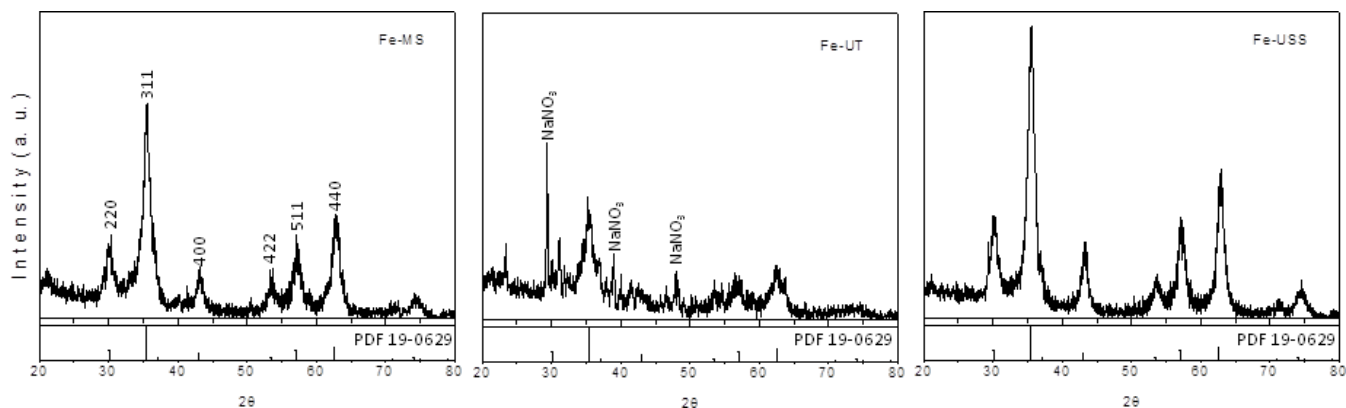


Figure 2. Effect of stirring method on the structural characteristics of Fe_3O_4 nanoparticles.

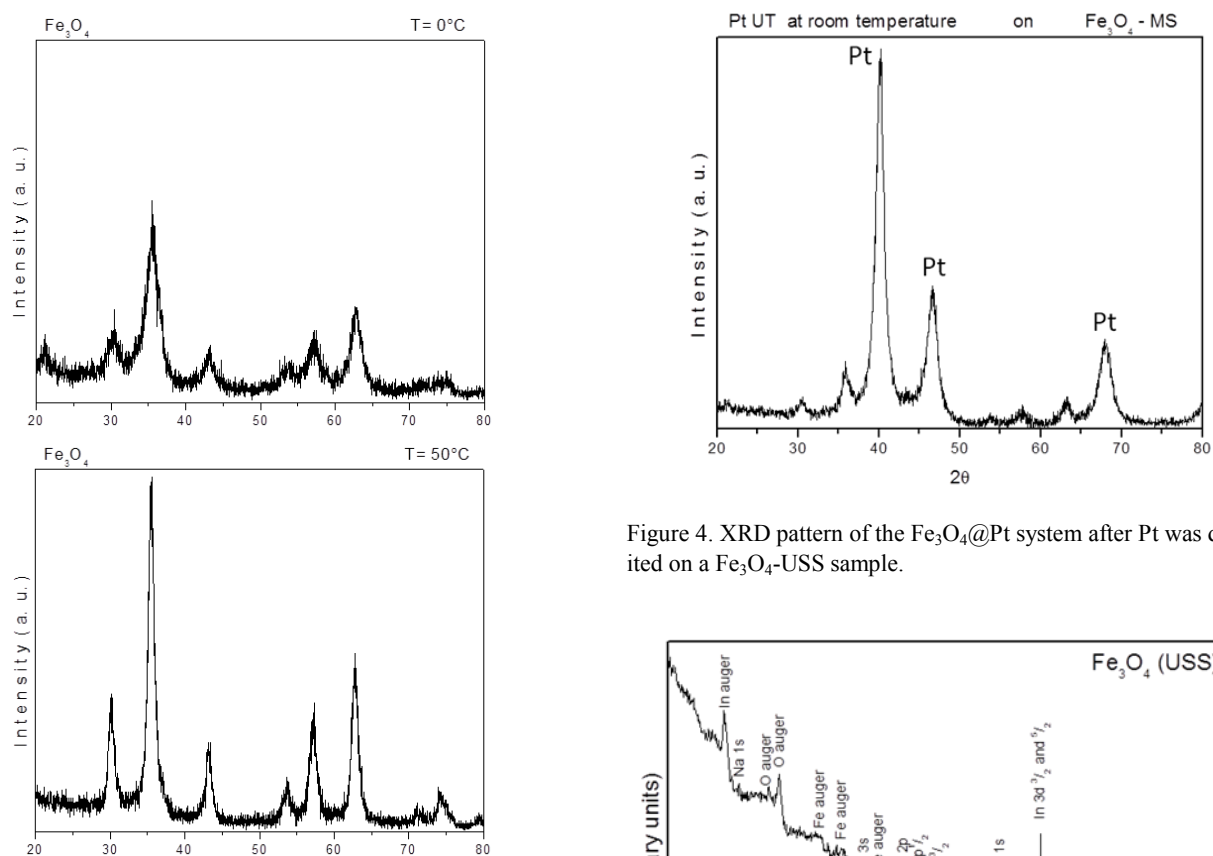


Figure 4. XRD pattern of the $Fe_3O_4@Pt$ system after Pt was deposited on a Fe_3O_4 -USS sample.

Figure 3. Effect of the synthesis temperature on the crystallinity of Fe_3O_4 nanoparticles.

The effect of reducing and increasing the synthesis temperature on the crystallinity of the magnetite nanoparticles is shown in Figure 3 for Fe_3O_4 -UT. When the temperature is higher (i.e., 50 °C) the crystallite size is larger than the size at RT and 0 °C. The magnitude of this change in crystallite size as a function of the synthesis temperature is more important when the reaction takes place over RT and less significant when the temperature is below RT. While the crystallite size grows up from 5.3 nm at RT to 9.2 nm at

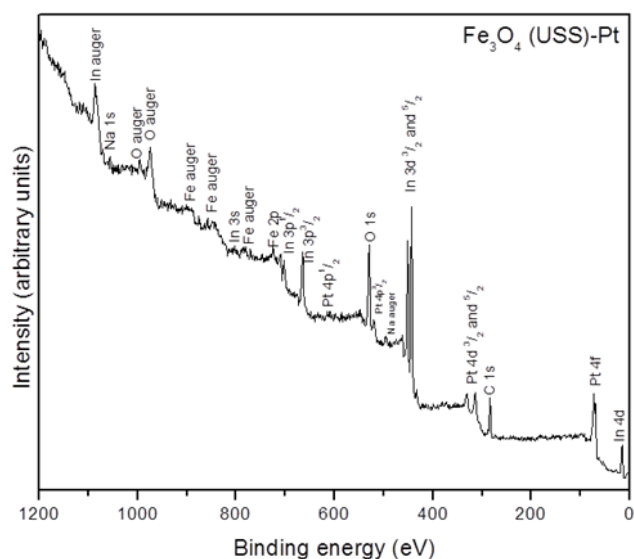


Figure 5. Photoelectron line positions of the Fe_3O_4 (USS)-Pt nanostructure.

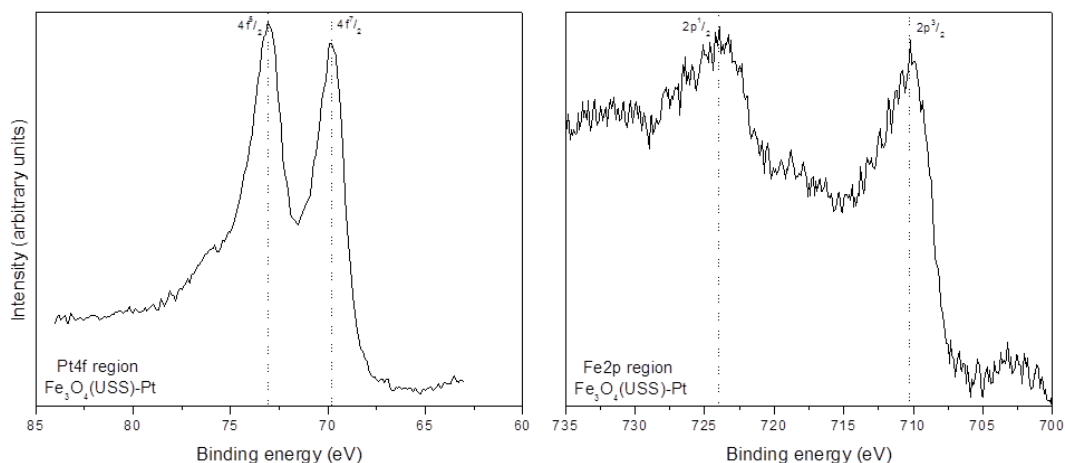


Figure 6. Pt 4f (left) and Fe 2p (right) XPS spectra of the $\text{Fe}_3\text{O}_4(\text{USS})\text{-Pt}$ nanostructure.

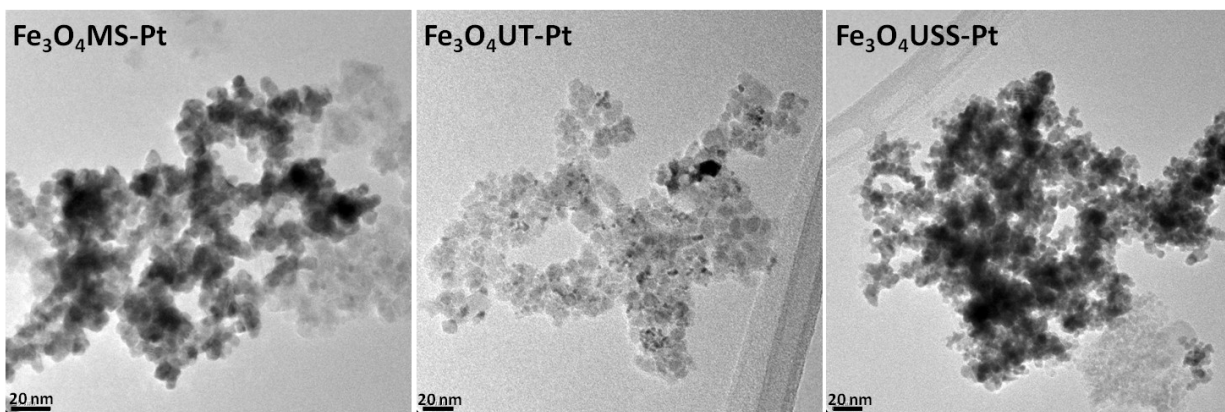


Figure 7. TEM micrographs of the $\text{Fe}_3\text{O}_4\text{@Pt}$ synthesized using MS, UT and USS stirring.

50 °C, the crystallite size is only reduced to 4.4 nm at 0 °C.

Pt was deposited on $\text{Fe}_3\text{O}_4\text{-MS}$, $\text{Fe}_3\text{O}_4\text{-UT}$ and $\text{Fe}_3\text{O}_4\text{-USS}$ samples. As an example of the structure of the core-shell materials, Figure 4 shows the XRD pattern of a $\text{Fe}_3\text{O}_4\text{@Pt}$ nanostructure synthesized using the $\text{Fe}_3\text{O}_4\text{-MS}$ sample. It is clearly demonstrated that through this simple synthesis route, Pt is rapidly deposited (after one minute stirring) on the magnetite nanoparticles by using the UT method. It can be observed that the $\text{Fe}_3\text{O}_4(\text{MS})\text{@Pt}$ nanostructure shows the two reflections sets, i.e., those associated to the magnetite structure and the main peaks related to the cubic close-packed structure of platinum, PDF 4-0802. This is considered to be a result of the large differences between both crystal structures and their cell parameters. It was found that the crystallite size of Pt in the three core-shell nanostructures, also calculated with the Scherrer equation, is around 7 nm.

The XPS spectra of the samples show the presence of the typical signals associated to the metallic elements used in these experiments for the three stirring methods, Pt and Fe. In addition to these peaks, the signals of indium (used as a support), carbon and oxygen (from the atmosphere) appear in the spectra.

An example of the XPS results collected from the core-shell

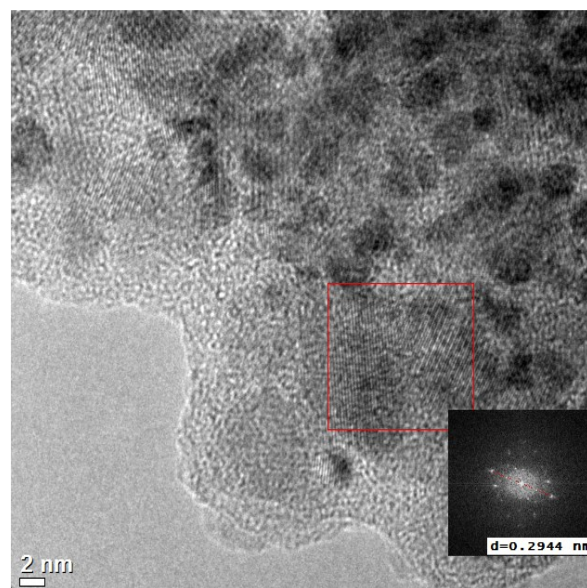


Figure 8. HRTEM of the $\text{Fe}_3\text{O}_4(\text{UT})\text{@Pt}$ nanostructure.

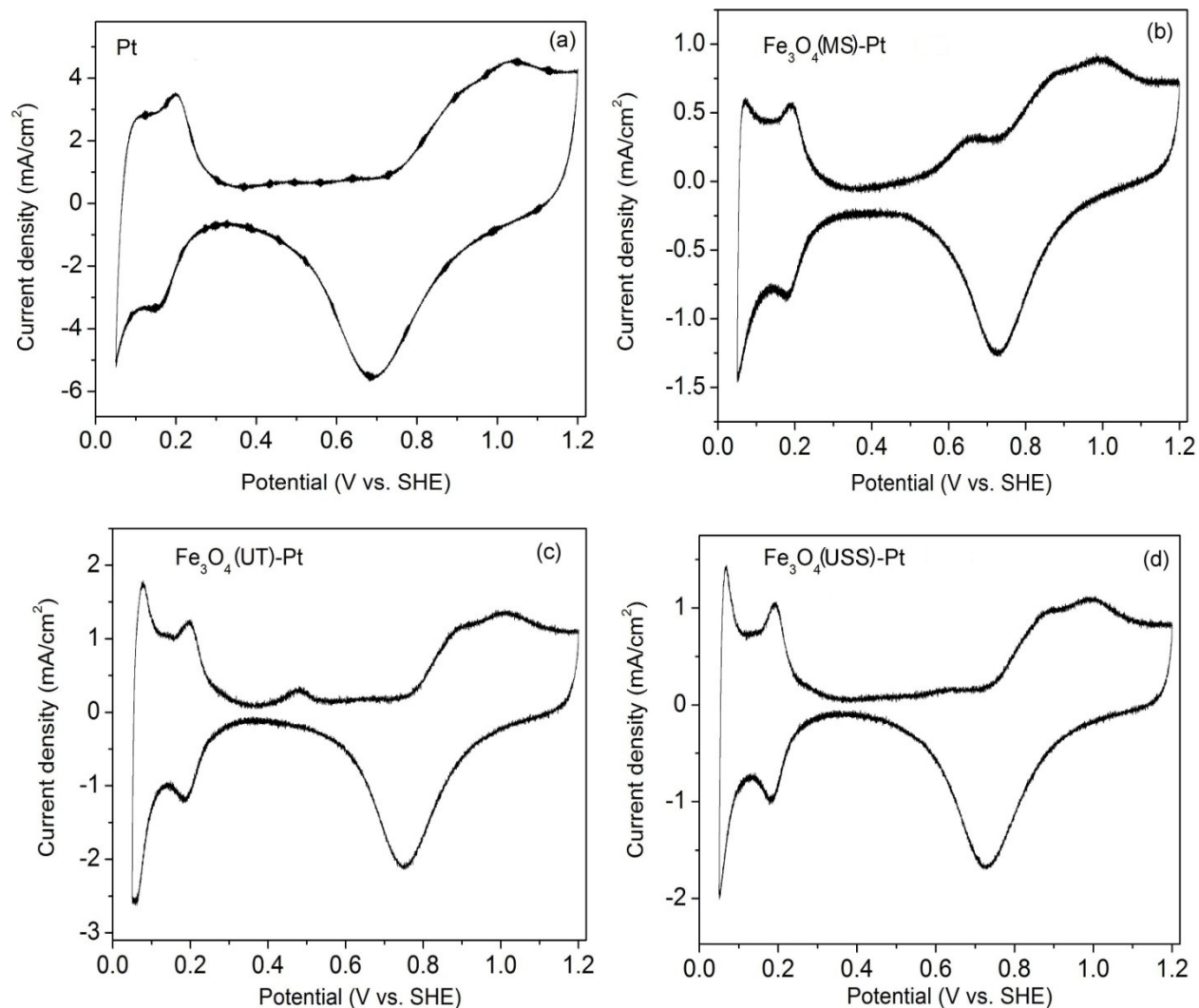


Figure 9. Voltammetry curves of the Pt nanoparticles (a) and the three $\text{Fe}_3\text{O}_4\text{-Pt}$ nanostructures (b-d). Electrolyte: N_2 -saturated 0.5M H_2SO_4 . Scan rate: 20 mV/s.

nanostructures is shown in Figure 5, where the spectra of $\text{Fe}_3\text{O}_4\text{(USS)@Pt}$ can be observed. It is important to remark that the Pt crystallite size, calculated from XRD analysis, is less than the penetration distance of the XPS equipment (10 nm) [14].

The XPS spectra corresponding to Pt 4f (left) and Fe 2p (right) are shown in Figure 6. The binding energies of the two signals of Pt 4f $7/2$ and $5/2$, with characteristic energies of 69.8 and 73.1 eV, respectively, have good concordance with those reported for samples of pure Pt [15]. Particularly, the Pt 4f $7/2$ peak confirms the presence of metallic Pt [13, 15 and 16]. On the other hand, the two peaks on the Fe 2p region could be assigned by comparing our results with the reported values for Fe, Fe_2O_3 and Fe_3O_4 [14]. The binding energy values characteristics of iron oxide in the $\text{Fe}_3\text{O}_4\text{(USS)@Pt}$ sample are 723.9 (2p $1/2$) and 710.3 (2p $3/2$) eV. After considering the shift due to the experimental conditions, it is possible to match the analyzed nanostructures with both Fe_3O_4 and Fe_2O_3 , due to the fact that Fe^{2+} and Fe^{3+} show the same behavior [14]. An indirect way to differentiate Fe_3O_4 from Fe_2O_3 is by meas-

uring the magnetic properties of the sample. While Fe_3O_4 has a ferrimagnetic behavior, Fe_2O_3 has antiferromagnetic properties. So, from the magnetic characteristics of $\text{Fe}_3\text{O}_4\text{(USS)@Pt}$ it is possible to determine the iron oxide phase in our catalyst.

Figure 7 shows the TEM images of the core-shell catalysts. In all three cases, nanoparticles with a size between 5 and 25 nm are formed and the material tend to develop agglomerates. This is typically seen in magnetic nanoparticles, although this characteristic is less clear in the case of the $\text{Fe}_3\text{O}_4\text{(UT)@Pt}$ sample.

The direct observation of core-shell structures through TEM analysis has been acknowledged to be complicated, in spite of the evidence of selectively deposition of Pt or Pt alloys on nanoparticles surface [9]. However, analysis by high resolution TEM (HRTEM) can give more detailed information and is a very useful tool to discern the morphology of core-shell materials [5]. For this reason, the samples were studied by HRTEM where clear lattice fringes can be observed.

Figure 8 shows the HRTEM analysis of the $\text{Fe}_3\text{O}_4\text{(UT)@Pt}$ sam-

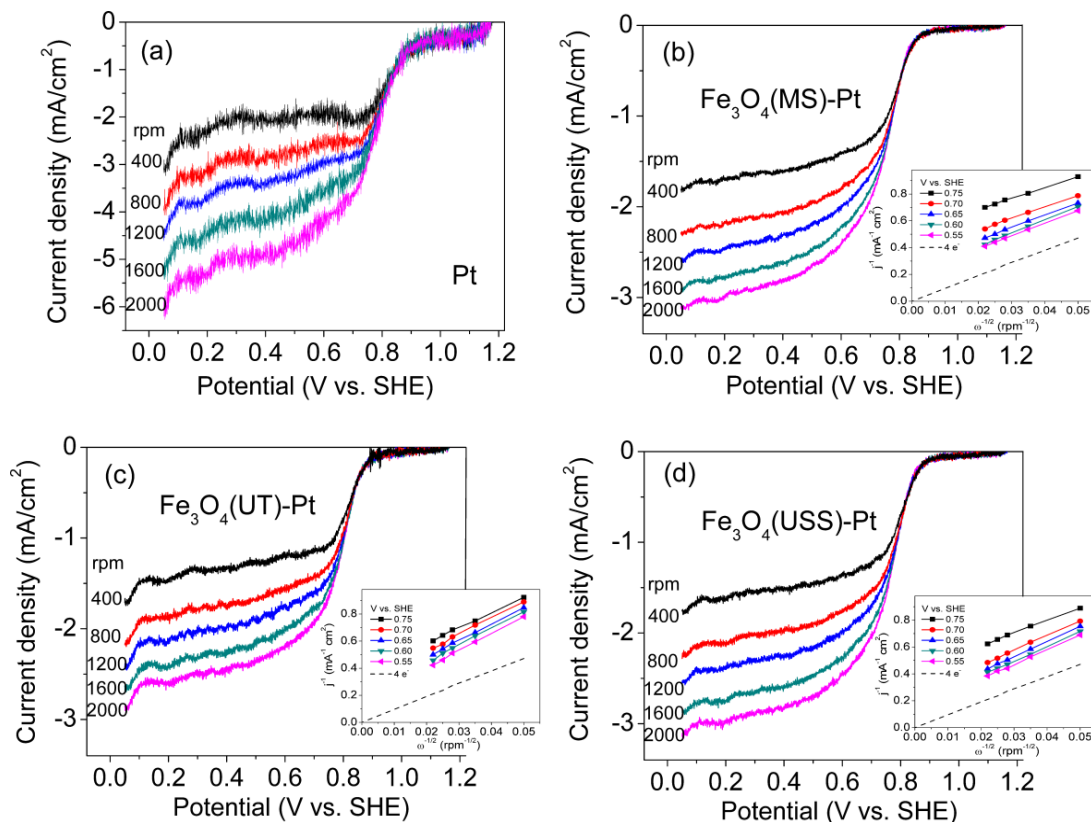


Figure 10. Linear scan voltammograms of the ORR at Pt (a) and the Fe_3O_4 -Pt nanostructures (b-d). Electrolyte: O_2 -saturated 0.5M H_2SO_4 . Scan rate: 2 mV/s.

ple. The image develops the presence of some sets of lattice planes. The distance between two adjacent planes of the $\text{Fe}_3\text{O}_4(\text{UT})@\text{Pt}$ material is 2.945\AA . This value reflects a lattice dilatation with respect to reported value of 2.532\AA for Fe_3O_4 [PDF 19-0629]. This confirms that the observed $\text{Fe}_3\text{O}_4(\text{UT})$ core nanoparticles have been covered by the Pt shell. The crystalline feature of the material is confirmed by the selected area electron diffraction pattern inserted in the Figure. The morphology of the nanoparticles show an outer layer with different contrast, ascribed to Pt deposited on the iron oxide core, in good agreement with previous reports in the literature [5].

Figure 9 shows the CVs of the Pt nanoparticles synthesized by UT and the $\text{Fe}_3\text{O}_4@\text{Pt}$ nanostructures (Fe_3O_4 synthesized by the three methods, Pt deposited by UT). All the figures clearly show the typical characteristics of Pt-containing materials, i.e., hydrogen, double layer and oxides regions. Such features observed in Figs. 9(b) to 9(d) confirm the deposition of Pt on the Fe_3O_4 cores, and

corroborate the XRD and HRTEM results in Figures 4 and 8, respectively.

The real surface area of the electrocatalysts (S , in cm^2_{Pt}) can be obtained by dividing the charge measured in the hydrogen desorption regions (Q_{H-des} in μC) in the CVs of Figure 9 after correction for double layer charging by the charge required for full coverage of a polycrystalline Pt electrode ($Q_H = 210 \mu\text{C cm}^2_{\text{Pt}}$). Moreover, the electrochemically active surface area (ECSA, in $\text{m}^2/\text{g}_{\text{Pt}}$) can be calculated using the equation [17, 18]:

$$ECSA = \frac{Q_{H-des}}{Q_H \cdot L_{Pt} \cdot A_g} \quad (1)$$

where L_{Pt} is the Pt loading ($\mu\text{g}_{\text{Pt}} \text{cm}^{-2}$) and A_g is the geometrical area of the disc support (cm^2). The real surface area, the ECSA and other characteristics of the different core@shell electrocatalysts are

Table 1. Characteristics of the Pt and core@shell electrocatalysts

Electrocatalysts	L_{Pt} ($\mu\text{g}_{\text{Pt}}/\text{cm}^2$)	S (cm^2)	ECSA ($\text{m}^2/\text{g}_{\text{Pt}}$)	i_s (0.9 V) ($\mu\text{A}/\text{cm}^2_{\text{Pt}}$)	i_m (0.9 V) ($\text{A}/\text{mg}_{\text{Pt}}$)
Pt	510	35	35.72	247.99	0.00136
$\text{Fe}_3\text{O}_4(\text{MS})-\text{Pt}$	255	3	7.57	267.79	0.00040
$\text{Fe}_3\text{O}_4(\text{UT})-\text{Pt}$	255	10	21.86	210.29	0.00091
$\text{Fe}_3\text{O}_4(\text{USS})-\text{Pt}$	255	8	16.00	145.30	0.00046

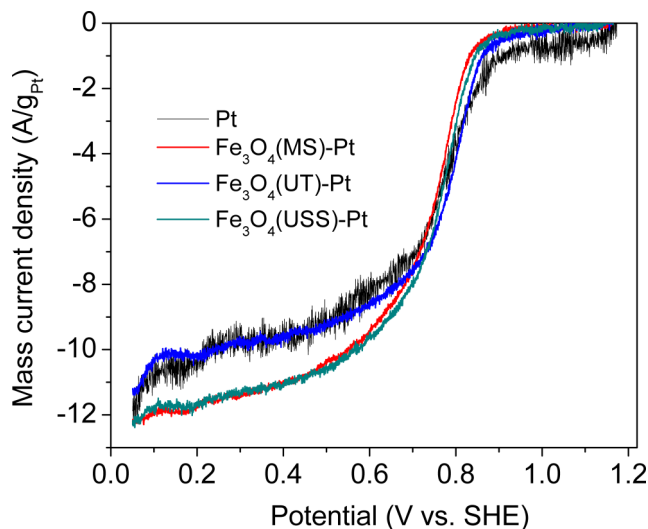


Figure 11. Mass specific polarization curves of the ORR at the Pt nanoparticles and the three $\text{Fe}_3\text{O}_4\text{-Pt}$ nanostructures, plotted considering the Pt content in the electrodes. Scan rate: 2 mV/s. ω : 2000 rpm.

presented in Table 1. As can be inferred from the hydrogen regions in Figure 9, the Pt nanoparticles show a larger S value (35 cm^2), followed by the $\text{Fe}_3\text{O}_4(\text{UT})@\text{Pt}$ and the $\text{Fe}_3\text{O}_4(\text{USS})@\text{Pt}$ nanostructures. The smaller S corresponds to $\text{Fe}_3\text{O}_4(\text{MS})@\text{Pt}$. All the electrocatalysts show an S value larger than the geometrical area of the support. The $ECSA$ values calculated from Eq. (1) are also presented in Table 1. Evidently, the Pt nanoparticles show a larger $ECSA$ ($35.72 \text{ m}^2/\text{g}_{\text{Pt}}$) than the core-shell nanostructures (for example, $21.86 \text{ m}^2/\text{g}_{\text{Pt}}$ was calculated for the $\text{Fe}_3\text{O}_4(\text{UT})@\text{Pt}$ nanostructure).

Figure 10 shows the LSVs of the ORR at the Pt nanoparticles (Fig. 10a) and the $\text{Fe}_3\text{O}_4@\text{Pt}$ core-shell nanostructures (Figs. 10b to 10d). In all cases, the current density (calculated considering $A_g = 0.196 \text{ cm}^2$) increases as a function of the rotation rate. The behavior of the three core-shell nanostructures is analogous during the polarization, i.e., the onset potential of the ORR is nearly 0.9 V vs. SHE and the current density at each ω value can be considered of comparable magnitude in all three cases. Such behavior suggests that the physicochemical and morphological characteristics of the nanostructures synthesized by the three stirring methods are quite similar and therefore they show almost the same performance as cathodes for the ORR. One important feature that must be evaluated when testing ORR cathodes is the number of electrons transferred during the reaction. As it is well known, a reaction approaching a $4 e^-$ transfer mechanism will give a full reduction of oxygen into H_2O , while a transfer of $2 e^-$ will produce H_2O_2 [19]. The insets in Figs. 10(b) to 10(d) depict the Koutecky-Levich plots of each of the core-shell nanostructures at different potentials. The theoretical slope corresponding to a $4 e^-$ ORR mechanism is also presented as a reference. Clearly, the experimental slopes of the core-shell cathodes correlate well with the theoretical slope, suggesting that the ORR taking place on these novel materials approaches a $4 e^-$ transfer mechanism.

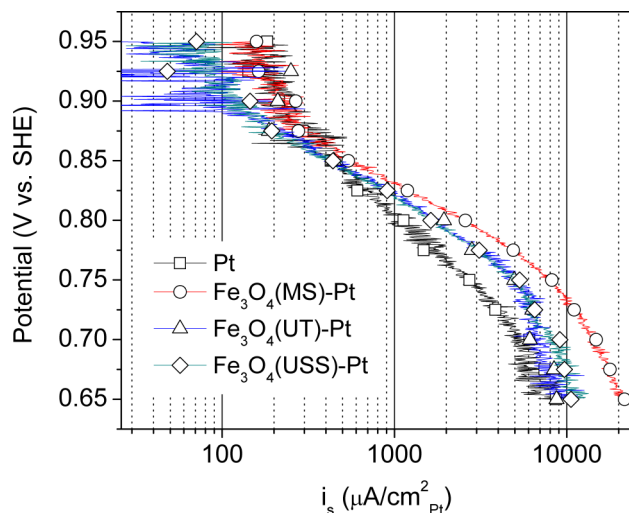


Figure 12. Specific activities of the Pt nanoparticles and the three $\text{Fe}_3\text{O}_4\text{-Pt}$ nanostructures, plotted considering the Pt real surface area and the Pt loadings. The ORR data used for this plots are those of Fig. 10 at $\omega=2000$ rpm.

The current density reached by the Pt-alone cathode in Figure 10 is higher than those of the core-shell materials. However, a different way to compare the results can be expressed by considering the Pt mass specific activity of the electrodes, i.e., the Pt content in grams [20]. Figure 11 shows the ORR mass specific current density of the four cathodes under $\omega=2000$ rpm. The specific activity of the three core-shell cathodes is similar to that of the Pt-alone nanoparticles. Even more, the $\text{Fe}_3\text{O}_4(\text{MS})@\text{Pt}$ and $\text{Fe}_3\text{O}_4(\text{USS})@\text{Pt}$ cathodes show a slight increase in mass specific current density at potentials more negative than 0.75 V vs. SHE compared to the current density of Pt.

A more detailed comparison of the catalytic activity of the core-shell cathodes and the Pt nanoparticles for the ORR can be done by plotting specific activities and mass activities. This is performed by correcting the measured ORR data for mass transport according to the following equation [17]:

$$i_k = \frac{i_d i}{i_d - i} \quad (2)$$

where i_k the mass-transport corrected kinetic current, i is the measured ORR current and i_d is the measured diffusion-limited current [17].

The specific current (i_s) is calculated normalizing i_k obtained from Eq. (2) with the Pt surface area and the Pt loading [17, 18]. Both parameters are presented in Table 1 for each electrocatalyst. Figure 12 shows the i_s vs. potential plots for the 4 different cathodes. The ORR current data used in such plots is that of Figure 10 at $\omega=2000$ rpm. Overall, from the results in Figure 12 it may be concluded that the specific activities of the Pt nanoparticles and the core-shell materials are similar. i_s values at 0.9 V are presented in Table 4. The $\text{Fe}_3\text{O}_4(\text{MS})\text{-Pt}$ cathode presents a higher specific activity at this potential than Pt-alone, while the lowest activity is that of $\text{Fe}_3\text{O}_4(\text{USS})@\text{Pt}$. It can be mentioned that the i_s values obtained

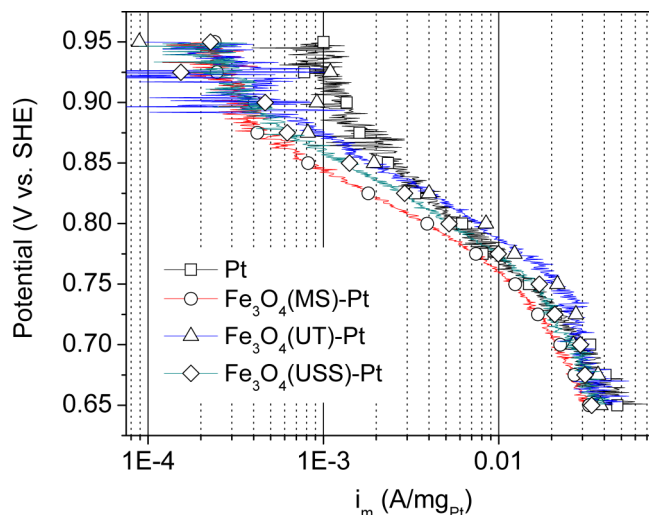


Figure 13. Mass activities of the Pt nanoparticles and the three Fe_3O_4 -Pt nanostructures, plotted considering the Pt loading. The ORR data used for this plots are those of Fig. 10 at $\omega = 2000$ rpm.

from our 4 cathodes is of the same order as that reported in the literature [17].

From the same ORR current data of Figure 10, it is possible to determine the mass activities of the nanomaterials. Calculating i_k and normalizing it to the Pt loading, i_m is obtained. Figure 13 shows mass activity plots of the four cathodes. At low overpotentials (0.95 to 0.85 V), the Pt nanoparticle shows a higher activity than the rest of the cathodes. However, for the rest of the polarization the mass activities of the four electrocatalysts are about the same. i_m values at 0.9 V for the four systems are presented in Table 1, indicating the higher activity of Pt. The results shown in Figures 11-13 indicate that Fe_3O_4 @Pt nanostructures with a reduced amount of Pt (i.e., lower price) can reach activities for the ORR as high as that of pure Pt electrodes.

Even though the dissolution of Fe_3O_4 in strong acid solutions has been mentioned previously [21], some reports indicate that the solubility of iron oxides in sulfuric acid may be low [22]. Moreover, it has been demonstrated that the surface modification of Fe_3O_4 by coatings with higher chemical stability, i.e. carbon, reduce its tendency to dissolve in 0.5 M H_2SO_4 [23]. Thus, one of the functions of the Pt shell deposited over the iron oxide core must be to avoid its dissolution. After confirmation of a high catalytic activity of the Fe_3O_4 @Pt system for the ORR, the next step is to evaluate the long-term durability of the nanostructure [24]. This can be done by applying potential cycles between 0.6 and 1.2 V vs. SHE, at the scan rate of 50 mV/s at room temperature. Then, the losses in surface area can be evaluated by performing CVs at 20 mV/s.

Figure 14 shows the CVs of Fe_3O_4 @Pt in N_2 saturated solution before and after 500 potential cycles. Clearly, the surface area loss in the hydrogen adsorption-desorption region is not significant after cycling, related to the surface area before the polarization test. A difference can be observed at high polarization potentials, where the formation of oxides is lower in the CV measured after cycling. Moreover, a slight shift of nearly 20 mV towards more positive potentials of the Pt oxide reduction peak can be observed in the

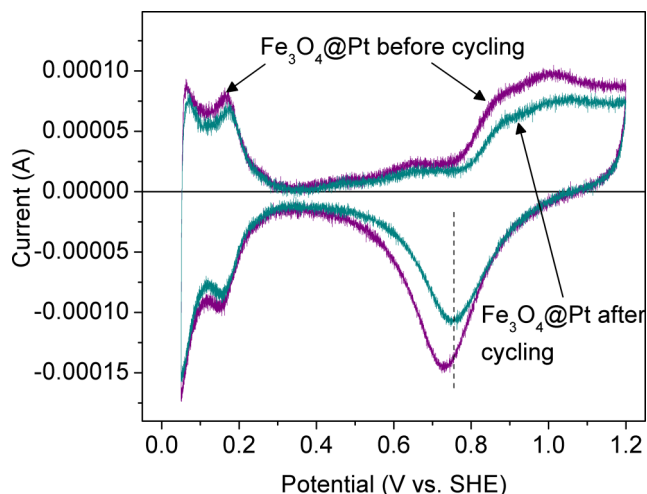


Figure 14. CVs of the Fe_3O_4 @Pt system acquired at 20 mV/s, before and after 500 polarization cycles between 0.6 and 1.2 V vs. SHE at the scan rate of 50 mV/s, at room temperature.

curve taken after polarization compared to the CV before cycling. A shift of this type has been attributed to a decrease of the desorption free energy (ΔG_{ads}) of Pt-OH, Pt-O or Pt-O₂, i.e., a lower adsorption strength of adsorbed oxygen species on Pt [25]. From the results in Figure 14, it can be concluded that the Fe_3O_4 @Pt system shows a high stability in 0.5 M H_2SO_4 , indicating that a Pt shell effectively covers the Fe_3O_4 core, avoiding its dissolution. The results presented here open the opportunity of evaluating the use of relatively cheap iron oxides along with low amounts of Pt to produce low-cost high performance cathodes in a core-shell nanostructure.

4. CONCLUSIONS

In this work we synthesized Fe_3O_4 and Pt nanoparticles, as well as Fe_3O_4 @Pt core-shell nanostructures by using three different stirring methods. The process of synthesis was easy to implement and fast, i.e., only one minute stirring time. In spite of that, we managed to obtain materials with a crystalline structure. We studied also the effect of changing the synthesis temperature on the physical properties of Fe_3O_4 . It was found that an increase of temperature to 50 °C (from the RT of 25 °C) increased the crystallite size, while a synthesis temperature of 0 °C resulted in a smaller size.

Crystallite sizes of 5-8 nm for the nanoparticles and 7 nm for the core-shell nanostructures were determined from XRD measurements. Also with this technique, the deposition of Pt on Fe_3O_4 was established. TEM analysis showed the formation of agglomerates and indicated a crystallite size of the nanostructures between 5 and 25 nm. Moreover, HRTEM studies confirmed the formation of the core-shell nanostructures. Meanwhile, XPS analysis indicated the presence of metallic Pt and the Fe_3O_4 phase in the core-shell electrocatalyst.

Electrochemical measurements were performed on the nanomaterials. The shape of the CVs obtained from the core-shell electrodes confirmed the presence of Pt. The analysis of hydrogen de-

sorption region indicated larger ECSA values for the Pt nanoparticles, followed by the Fe₃O₄(UT)@Pt core-shell cathode.

When evaluated as cathodes for the ORR, the core-shell materials showed a high electrocatalytic activity, with an onset potential of nearly 0.9 V. A more detailed analysis confirmed that the specific and mass activities of the Fe₃O₄@Pt electrodes were of the same magnitude as that of the Pt-alone nanoparticles. Such results confirmed that Fe₃O₄@Pt core-shell cathodes with lower Pt content can sustain a performance as high as that of a pure Pt cathode, but with a lower price. The durability tests performed on the Fe₃O₄@Pt systems indicate that the material is stable in 0.5 M H₂SO₄ with insignificant surface area losses, confirming that the Pt shell efficiently covers the iron oxide core, avoiding its dissolution. These results can lead to the formulation of low-cost cathodes formed by cheap iron oxides and a small amount of Pt in a core-shell configuration.

5. ACKNOWLEDGMENTS

The authors thank the Mexican National Council for Science and Technology (CONACYT) for financial support through grant 79870 and the Programa de Redes Temáticas.

REFERENCES

- [1] S. Alayoglu, A.U. Nilekar, M. Mavrikakis, B. Eichhorn, *Nature Materials*, 7, 333 (2008).
- [2] H. Wang, C. Xu, F. Cheng, M. Zhang, S. Wang and S.P. Jiang, *Electrochem. Commun.*, 10, 1575 (2008).
- [3] N.V. Long, T. Asaka, T. Matsubara and M. Nogami, *Acta Materialia*, 59, 2901 (2011).
- [4] K. Sasaki, J.X. Wang, H. Naohara, N. Marinkovic, K. More, H. Inada and R.R. Adzic, *Electrochim. Acta*, 55, 2645 (2010).
- [5] G. Wang, H. Wu, D. Wexler, H. Liu and O. Savadogo, *J. Alloy Compd.*, 503, L1 (2010).
- [6] Hui Wang, Rongfang Wang, Hao Li, Qunfang Wang, Jian Kang and Ziqiang Lei, *Int. J. Hydrogen Energy*, 36, 839 (2011).
- [7] Yuan Wang and Naoki Toshima, *J. Phys. Chem. B*, 101, 5301 (1997).
- [8] Rongfang Wang, Hui Wang, Bangxing Wei, Wei Wang, Ziqiang Lei, *Int. J. Hydrogen Energy*, 35, 10081 (2010).
- [9] Haili Gao, Shijun Liao, Jianhuang Zeng, Yichun Xie, Dai Dang, *Electrochim. Acta*, 56, 2024 (2011).
- [10] D. Kaplan, M. Alon, L. Burstein, Yu. Rosenberg and E. Peled, *J. Power Sources*, 196, 1078 (2011).
- [11] Nguyen Viet Long, Michitaka Ohtaki, Tong Duy Hien, Jalem Randy and Masayuki Nogami, *Electrochim. Acta*, 56, 9133 (2011).
- [12] D. Morales-Acosta, L.G. Arriaga, L. Alvarez-Contreras, S. Fraire Luna and F.J. Rodríguez Varela, *Electrochem. Commun.*, 11, 1414 (2009).
- [13] F.J. Rodríguez Varela, A.A. Gaona Coronado, J.C. Loyola, Qi-Zhong Jiang and P. Bartolo Perez, *J. New Mat. Electrochem. Systems*, 14, 75 (2011).
- [14] Jerome Leveueur, Geoffrey I.N. Waterhouse, John Kennedy, James B. Metson and David R.G. Mitchell, *J. Phys. Chem. C*, 115, 20978 (2011).
- [15] A.S. Arico, A.K. Shukla, H. Kim, S. Park, M. Min, V. Antonucci, *Applied Surface Science*, 172, 33 (2001).
- [16] Lei Shen, Qi-Zhong Jiang, Tao Gan, Min Shen, F.J. Rodríguez Varela, A.L. Ocampo and Zi-Feng Ma, *J. New Mat. Electrochem. Systems* 13, 205 (2010).
- [17] Hubert A. Gasteiger, Shyam S. Kocha, Bhaskar Sompalli, Frederick T. Wagner, *Appl. Catal. B: Environm.* 56, 9 (2005).
- [18] Yannick Garsany, Olga A. Baturina, Karen E. Swider-Lyons and Shyam S. Kocha, *Anal. Chem.*, 82 6321 (2010).
- [19] N.M. Markovic, T.J. Schmidt, V. Stamenkovic and P.N. Ross, *Fuel Cells*, 1, 105 (2001).
- [20] Seth L. Knupp, Miomir B. Vukmirovic, Pradeep Haldar, Jeffrey A. Herron, Manos Mavrikakis and Radoslav R. Adzic, *Electrocatal.*, 1, 213 (2010).
- [21] Lirong Kong, Xiaofeng Lu, Xiujie Bian, Wanjin Zhang, and Ce Wang, *Appl. Mat. Interf.*, 3, 35 (2011).
- [22] Document Chemical Cleaning of Metals, (nzic.org.nz/ChemProcesses/metals/8H.pdf), consulted on January 2012.
- [23] Linfei Lai, Guoming Huang, Xiaofeng Wang, Jian Weng, *Carbon*, 49, 1581 (2011).
- [24] Kotaro Sasaki, Kurian A. Kuttiyiel, Dong Su, Radoslav R. Adzic, *Electrocatal.*, 2, 134 (2011).
- [25] L.G.R.A. Santos, C.H.F. Oliveira, I.R. Moraes, E.A. Ticianelli, *J. Electroanal. Chem.*, 596, 141 (2006).